ADVANCED OPTICAL MATERIALS
www.advopticalmat.de

Multi-fold Phase Metasurface Holography Based on Frequency and Hybrid Decoupling Polarizations

Hongqiang Zhou, Chongli Zhao, Cong He, Qiang Jiang, Hongbo Wang, Ruizhe Zhao, Tianlong Man, Yuhong Wan, Guangzhou Geng,* and Lingling Huang**

Metasurfaces are artificially intelligent planar optical devices that can realize excellent functions by optimizing the design of nanostructures and arrays. Metasurfaces have become the preferred approach for fabricating integrated and compact optical systems with micro- and nano-scale solutions for realizing multi-dimensional modulated optical devices. Herein, the realization of multi-fold phase holography is demonstrated by combining switchable optical frequencies with hybrid circular and linear polarization states. The original holographic phase distribution can be inversely optimized using an adaptive momentum gradient descent algorithm. Furthermore, completely different images can be reconstructed when the phase values are several times the original values. The multi-fold phase modulation can be achieved by optimizing the structural distribution of the dielectric metasurface with the incident changeable light frequency and decoupled circular and linear polarization. Different polarization combinations enhance the flexibility of multiple holographic modulations. This technology provides new solutions for dynamic multi-fold beam directional refraction and excitation, orbital angular momentum communication, multi-fold holographic displays, optical encryption and camouflage, light switching, and shaping.

1. Introduction

The optical frequency, phase, and polarization state play important roles in modulating the degrees-of-freedom of light. In several fields, parameters such as optical frequency and polarization must be modulated for full-color holography or displays,[1] polarization cameras,[2–6] spectrometers,[7–9] and other applications.[10–12] Conventional optical components can control only a single variable, and complex systems must be integrated to achieve multi-parameter modulation. As a novel optical platform, metasurfaces can facilitate arbitrary optical field manipulation via elaborate engineering of meta-atoms, which represents a significant revolution in comparison with their 3D bulk metamaterial counterparts.[13–16] Metasurfaces with ultrathin planar sizes can control multiple degrees-of-freedom of light synchronously or asynchronously.[17–24] After extensive research and development, metasurfaces have been applied in multiple fields, including metalenses for visible and infrared imaging and telephoto detection,[25–29] optical computing,[30–34] optical neural networks,[35–38] holographic displays,[39–42] and nonlinear optics.[43–45] In particular, metasurface holography can address the challenges observed in conventional digital or optical holography using intelligent algorithms; these challenges include a large field of view, elimination of unnecessary diffraction, high-quality signal-to-noise ratio, and integration.

Previous studies on metasurface holography have reported that phase-type metasurfaces occupied a dominant position.[46–48] Multi-channel metasurfaces with a combination of amplitude,[49] polarization,[50–53] wavelength,[54,55] and other parameters can realize full-color or grayscale nano-printing and other excellent designs. The variable quantitative multi-fold phase can modulate beam refraction, optical switching, and holographic displays. However, achieving quantitative multi-fold phase modulation requires the stimulation of the nonlinear effects of nanofin arrays.[56] Thus far, the excitation of nonlinear effects on nanostructures has often required stringent experimental conditions, such as high laser power and extremely accurate antenna size. Moreover, the weak radiant power of harmonics increases the difficulty of detection, and the energy distribution is often unequal in multi-fold phase modulation when diffraction grating is used.

In this study, we propose a multi-fold phase holographic display strategy that can generate double-, triple-, six-fold, or other phase-only holography through the quantitative multiplication

H. Zhou, C. Zhao, T. Man, Y. Wan
School of Physics and Optoelectronic Engineering
Beijing University of Technology
Beijing 100124, China
E-mail: yhongw@bjut.edu.cn

C. He, Q. Jiang, H. Wang, R. Zhao, L. Huang
Beijing Engineering Research Center of Mixed Reality and Advanced Display
School of Optics and Photonics
Beijing Institute of Technology
Beijing 100081, China
E-mail: huanglingling@bit.edu.cn

G. Geng
Institute of Physics
The Chinese Academy of Sciences
Beijing 100191, China
E-mail: genggz@iphy.ac.cn

The ORCID identification number(s) for the author(s) of this article can be found under https://doi.org/10.1002/adom.202402303

DOI: 10.1002/adom.202402303

of a basic phase map. This utilizes a single dielectric metasurface with the hybrid decoupling of circular/linear polarizations and frequencies. We used the built-in adaptive momentum optimization (Adam) algorithm of TensorFlow (version 2.0) to construct a multi-fold phase hologram generation algorithm loop. Four completely different reconstructed images were obtained by optimizing the basic phase map and its multi-fold phase maps. The folded phase distributions were then assigned to different light frequencies and hybrid decoupling polarization state combinations. The metasurface achieved multi-fold phase holographic control by changing the frequency and polarization of the incident light. Four combinations of discrete light frequencies, circularly polarized light, and linearly polarized light were selected for phase-type holography. First, a metasurface was designed to determine the phase distribution of a circularly polarized decoupling combination at a wavelength of 800 nm; the left-handed circularly polarized channel modulated the basic phase map, whereas the right-handed circularly polarized channel served as a triple-phase modulator. Because the circular polarization modulation was based on the geometric phase decoupling principle, the rotation angles of the nanofins were determined. When the incident light was tuned to a wavelength of 1000 nm, the phase map was modulated at other times using orthogonal linear polarization decoupling channels. The horizontal linear polarization channel modulated the phase map twice, whereas the vertical linear polarization channel modulated the phase map six times. Therefore, a single metasurface realized schemes in which arbitrary multi-fold phase maps were quantitatively induced by the incident frequency and polarization. Such schemes can open up new possibilities for multi-fold phase modulation in optical computing, optical communication, dynamic holographic displays, and multifunctional integrated polarized imaging devices. We believe that the study can enhance the methods used for light phase modulation and significantly expand the applications and development scope of metasurfaces, providing valuable insights for the future design of holographic metasurfaces.

2. Methods and Results

Figure 1 depicts a schematic of multi-fold phase holography induced by frequency and polarization. The basic phase distribution is optimized using the Adam algorithm, and the K-fold phase can achieve a completely different reconstruction. The phase maps are then matched in different frequencies and polarization channels. The dielectric nanofin arrays were combined on the silica substrate, and two holograms were reconstructed by illuminating wavelength λ_1 in two cross-circular polarization channels (i.e., left-handed circular polarization (LCP) for incidence/transmission to the right-handed circular polarization (RCP) condition and vice versa). When the incident light wavelength changed to λ_2, these anisotropic rectangular nanofins functioned as phase contributors to the co-polarization channel for K-fold holograms. This scheme was experimentally verified by generating four different K-fold phase holographic images (K = 1, 3, 2, 6) in the near-infrared wavelength range in the cross-polarization channel (T_{rl}/T_{lr}, λ_1 = 800 nm) and co-polarization channel (T_{xx}/T_{yy}, λ_2 = 1000 nm).

The Adam optimization algorithm plays a vital role in generating the multi-fold phase hologram. We developed an optimization loop for generating multi-fold phase-only holograms (**Figure 2**). First, a random phase φ was generated and multiplied by different multiples of K, resulting in K-fold phases. Specifically, multi-fold holograms were obtained from the basic phase map multiplied by K-folds and wrapping. The obtained K-fold phases were used for holographic reconstruction. In general, holographic reconstruction from holograms to the object plane can be expressed using a Fourier transform. The mean squared errors (MSEs) of the four quantitatively reconstructed holograms were calculated using the ground truths as labels. The four MSEs were synchronously collected as metrics for phase updating in the optimization loop. This generated an optimized basic phase hologram via finite adaptive momentum calculations. The MSEs between the reconstructions and ground truths can be calculated as follows:

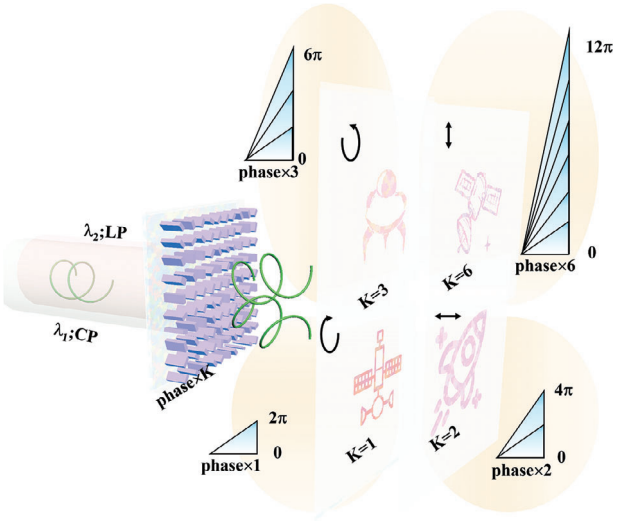

Figure 1. Concept of multi-fold phase holography induced by frequency and polarization. (LP: linear polarization; CP: circular polarization; and K: phase fold number).

$$E_r = \sum_i \left(\left| \Im \left(A e^{j\varphi_i} \right) \right|^2 - G_i \right)^2 \tag{1}$$

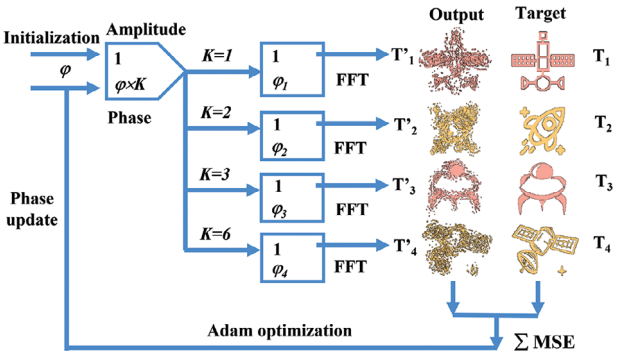

Figure 2. Principle of the multi-fold phase hologram algorithm. Adam optimization is the adaptive momentum estimation optimizer used for basic phase distribution.

where φ_i denotes the 2D phase distribution in the spatial domain; A represents the amplitude of the hologram, which is uniform with $A = 1$; $\mathfrak{F}$ indicates a 2D Fourier transform operation; and G_i represents the label. i means the number of holograms. The proposed algorithm serves as an efficient and straightforward approach for designing phase profiles for multi-fold phase metasurfaces.

According to the aforementioned loop algorithm, both the frequency and polarization were selected for multi-fold phase holographic demonstrations. When the illumination wavelength is incident on the metasurface, the output light field E_{out} is uniquely determined as expressed by the Jones matrix:

$$E_{out} = J(\theta) E_{in} \tag{2}$$

Each nanofin satisfies the unity matrix as a J-plate, and E_{in} represents circular polarization incidence, $E_{in} = \begin{bmatrix} 1 \\ \pm i \end{bmatrix}$. Owing to the application of circular and linear polarizations at two incident frequencies, the rotation angle of the nanofin (θ) on the metasurface can be determined for polarization conversion. Therefore, Equation (2) can be expressed as

$$E_{out} = R^{-1}(\theta)\, TR(\theta)\, E_{in} \tag{3}$$

where $R(\theta)$ denotes the rotation matrix of the J-plate, and $T = \begin{bmatrix} A_x e^{i\varphi_{xx}} & 0 \\ 0 & A_y e^{i\varphi_{yy}} \end{bmatrix}$ with $A_x e^{i\varphi_{xx}}$ and $A_y e^{i\varphi_{yy}}$ indicating the eigenvectors of the nanofins. Furthermore, each nanofin transmission can be inversely deduced using Equation (3), as follows:

$$T = R(\theta) E_{out} E_{in}^{-1} R^{-1}(\theta) \tag{4}$$

According to circular polarization decoupling, the RCP and LCP outputs exhibit completely independent phase distributions in the LCP and RCP incidences, respectively. Therefore, the target output light-field distributions E_{out} are endowed with K-fold phase holograms (K = 1, (φ_1); K = 3, (φ_3)). The decoupling phase satisfies the combination of the resonance and geometric phases. Therefore, the total number of phases can be expressed as follows:

$$\begin{aligned} \varphi_1 &= \varphi_0 + \varphi_{PB}\left(T_{rl800}\right) \\ \varphi_3 &= \varphi_0 - \varphi_{PB}\left(T_{lr800}\right) \end{aligned} \tag{5}$$

where φ_0 denotes the initial phase in the circular polarization illumination, φ_{PB} indicates the geometric phase obtained from the cross-polarization conversion, T_{rl} represents the RCP incidence and LCP output, and T_{lr} denotes the reverse polarization. The geometric phase introduced by circular polarization inversion is known to be a conjugate. The initial and geometric phases can be expressed using Equation (6).

$$\varphi_0 = \frac{\varphi_1 + \varphi_3}{2}; \varphi_{PB} = \frac{\varphi_1 - \varphi_3}{2} \tag{6}$$

The nanofin rotation angle was half of the geometric phase value. The other K-fold phase distributions were arranged using a new incident frequency. After obtaining the eigenvectors using Equation (4), the minimum phase differences between the transmission phases T_{xx} and T_{yy} of the nanofin (K = 2, ($\varphi_1 \times 2 = \varphi_2$); K = 6, ($\varphi_1 \times 6 = \varphi_4$)) were selected at diverse working light frequencies. The selected matrix value L can be presented as

$$L = \min\left(\left|\varphi_0 - \varphi_{rl800}\right| + \left|\varphi_2 - \varphi_{xx1000}\right| + \left|\varphi_4 - \varphi_{yy1000}\right|\right) \tag{7}$$

where min denotes the minimum value of the function, φ_{rl800} is the cross-circular polarization transmission at an incident wavelength of 800 nm, and φ_{xx1000} and φ_{yy1000} are the co-linear polarization transmissions at a wavelength of 1000 nm. The linear transmission phase could not be changed because of the confirmed rotation of the nanofin. Based on the above discussion, the decoupling minimum values were obtained via the phase differences between the cross-circular and linear polarization states at the two incident frequencies using Equations (4)–(7).

To satisfy the multi-fold phase modulation condition at the two frequencies, we swept the anisotropic structural parameters (**Figure 3a**). Anisotropic rectangular nanofins were selected with the length and width ranging from 80 to 300 nm. The geometric dimensions of each rectangular nanofin were determined considering its transmission phase, whereas the rotation angle was defined by its geometric phase. Full-wave simulations were conducted using the commercially available finite-difference time-domain method. We conducted a simulation analysis using the finite-difference time-domain (FDTD) method to explore flexion behavior with changes in geometric size. First, the lattice period was maintained at 450 nm, and the height of the anisotropic rectangular nanofins was set to 1000 nm. The lengths of the nanofins ranged from 80 to 300 nm, with a step size of 10 nm. Figure 3b,c illustrates the cross-circular polarization conversion intensity and phase maps at an incident wavelength of 800 nm. Figure 3d,e depicts the co-linear horizontal polarization intensity and phase maps at an incident wavelength of 800 nm. A silicon metasurface with a height of 1000 nm exhibits different transmittances at different incident wavelengths. Figure 3f,g depicts the co-linear horizontal polarization intensity and phase maps at an incident wavelength of 1000 nm. A comparison of Figure 3d,e and Figure 3f,g indicates that the metasurface exhibits a relatively large dispersion difference at incident wavelengths of 800 and 1000 nm. When the transmittance of the nanofin is high and a sufficient phase difference exists between the two distinct wavelengths, it is feasible to extend the selected frequency to other bands. Additionally, the metasurface exhibits relatively low transmittance at both discrete operating frequencies. This may be attributed to the lower transmission intensity of the nanofins in the array. Meanwhile, the phase modulation covers the entire range from 0 to 2π. The co-linear vertical polarization intensity and phase at an incident wavelength of 1000 nm indicate the transposition matrices of the horizontal polarization. The crosstalk between multi-fold phase holograms can be eliminated by optimizing the structure selection via polarization decoupling and by producing a large dispersion difference at the two incident frequencies. Therefore, the corresponding K-fold phase distributions were encoded using the aforementioned algorithms. In comparison with conventional metasurface holography, the space bandwidth product of metasurfaces is completely expanded by the sophisticated design.

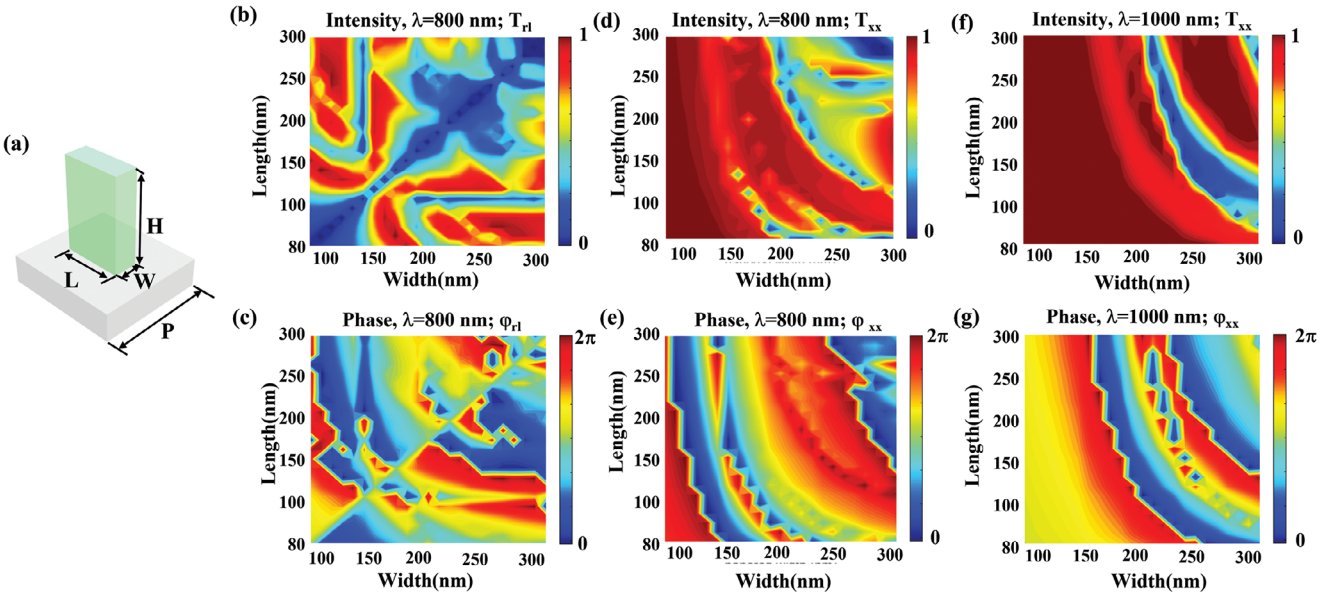

Figure 3. Nanostructural units and transmission maps. a) The concept of nanofins (H: height, W: width, L: length, and P: lattice constant). b,c) Cross-circular polarization transmission intensity and phase maps at an incident wavelength of 800 nm. d,e) Co-linear polarization transmission intensity and phase map of the swept length and width at an incident wavelength of 800 nm. f,g) Co-linear polarization transmission intensity and phase map of the swept length and width at an incident wavelength of 1000 nm.

For fabricated the sample, in the initial step, the first layer of the α-Si metasurface was crafted via electron beam lithography. Subsequently, a hard-etching mask of the Cr layer was deposited on the sample via electron gun evaporation, followed by a lift-off process. After the removal of the resist, the required patterns were transferred to the Cr mask, and the metasurface was obtained via reactive ion etching and removal of the patterned Cr mask. This was followed by Cr mask lift-off and dry etching. **Figure** 4a depicts the top view of the scanning electron microscopy (SEM) images. We measured the broadband transmittance curve of the metasurface in the cross-circular polarization and co-linear polarization channels (Figure 4b,c). Figure 4d illustrates the experimental optical configuration. A super-continuous laser was used as the light source (wavelength ranging from 680 to 1080 nm). When the incident light wavelength was λ_1, the combination of a linear polarizer and quarter-wave plate produced circularly polarized light, which impinged the metasurface. The K-fold holographic reconstructed image was observed in the far-field using the Fourier transform. When the wavelength of the light was switched to λ_2, the quarter-wave plates were removed, and the co-linear polarization transmissions were reconstructed in the far-field.

In the experiment, we found that Huygens phase modulation was shifting due to the sample fabrication error compared to the target incident wavelength. **Figure** 5 depicts the calculation and experimental reconstructions of K-fold holograms obtained to verify the design results. A twin-tailed satellite image was reconstructed in the far-field RCP-to-LCP channel (Figure 5a,e; K = 1) re-considering an illumination wavelength of 820 nm when sample measurement. Furthermore, the spaceship cartoon image was presented in the far-field LCP-to-RCP channel (Figure 5b,f; K = 3). We observed that the phase value of the spaceship's hologram was three times that of the twin-tailed satellite image. Additionally, other K-fold holographic reconstructions were presented in the far-field (Figure 5c,d,g,h; K = 2 and K = 6) in the horizontal (T_{xx}) and vertical (T_{yy}) co-polarization channels re-considering a wavelength of 930 nm when sample measurement. The rocket and disc-tail satellite images were displayed in co-linear polarization. We observed that the phase value of the rocket-hologram was double that of the twin-tailed satellite image, whereas the phase value of the disc-tail satellite-hologram was six times that of the twin-tailed satellite image.

Moreover, the efficiency of the fabricated metasurface at the target wavelength is relatively low. This can be attributed to the suboptimal transmittance of the selected nanofins at the target wavelength. The algorithm used for selecting nanofins can be optimized further as selecting nanofins with higher transmittance can enhance the transmission efficiency. Consequently, the proposed metasurface has the potential to achieve higher efficiency in the future, and we intend to refine the algorithm in subsequent work. Another factor influencing the target reconstruction efficiency is the inevitable appearance of zero-order spots in the reconstructed image of co-polarization holography during the co-polarization experiment. The background noise during the experiment was relatively large when the wavelength was 930 nm as the zero-order power of co-polarization channels played a major role in the analysis. This led to low target reconstruction efficiency, which in turn affected the quality of the reconstructed images in multi-fold holography to some extent. However, matching amplitude and phase errors can be simultaneously reduced and the strong zero-order beams can be suppressed during the experiment by adjusting the intensity ratio of different channel losses reconstructed by the algorithm. Moreover, the relatively higher quality of holographic reconstruction under cross-polarization may cause the issue of phase-matching accuracy, thereby contributing to the noise observed in the experimental results. The

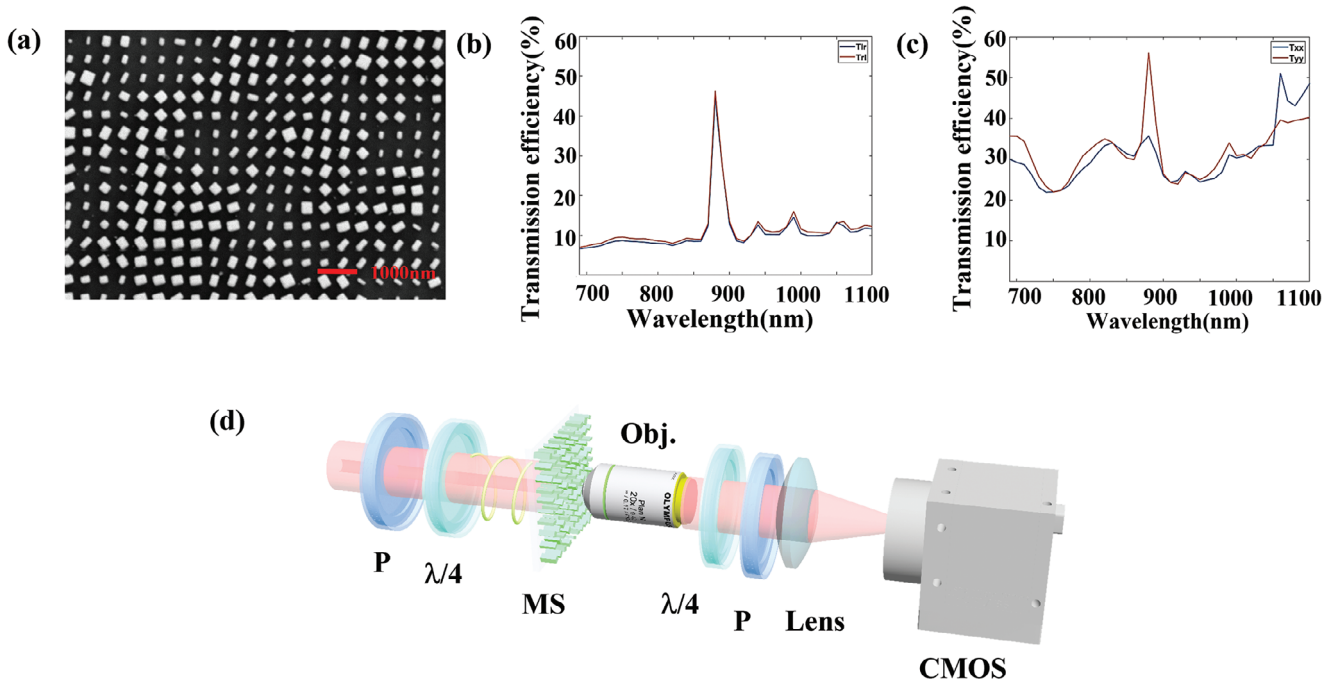

Figure 4. Metasurface sample and optical setup. a) Metasurface scanning electron microscopy (SEM) images (top view, scalebar: 1000 nm). b) The broadband transmission efficiency curve in cross-circular polarization channels (T_{rl}, T_{lr}). c) The broadband transmission efficiency curve in co-linear polarization channels (T_{xx}, T_{yy}). d) Experimental optical setup. (P: linear polarizer; $\lambda/4$: quarter-wave plate; and CMOS: complementary metal-oxide-semiconductor).

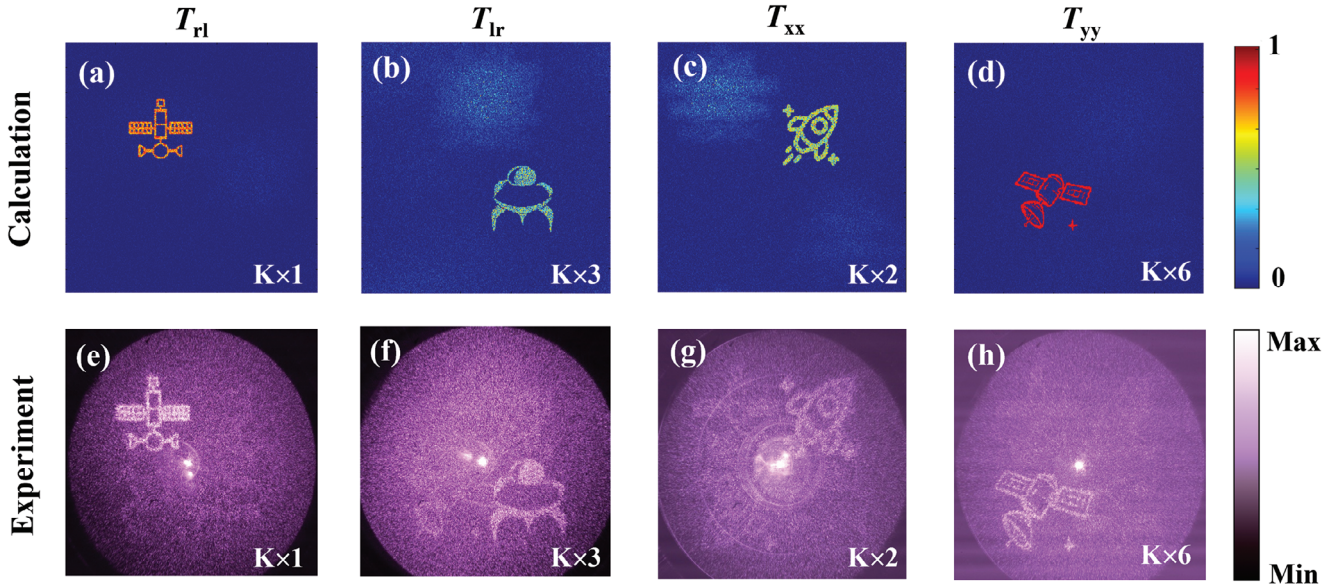

Figure 5. Simulations and experimental results of the multi-fold phase holograms obtained using dual-wavelength and polarization. a,e) The calculation and experimental reconstruction of basic (K = 1) holographic results in terms of cross-polarization (T_{rl}) at a wavelength of 820 nm. b,f) The calculation and experimental reconstruction of multi-phase (K = 3) holographic results in terms of cross-polarization (T_{lr}) at 820 nm. c,g) The calculation and experimental reconstruction of multi-phase (K = 2) holographic results in terms of co-polarization (T_{xx}) at 930 nm. d,h) The calculation and experimental reconstruction of multi-phase (K = 6) holographic results in terms of co-polarization (T_{yy}) at 930 nm.

laser speckle noise observed in the reconstructed image is universal because of the enhanced laser illumination coherence. The speckle noise observed during the experiment can be suppressed by reducing the laser coherence or by filtering the zero-order term. Nevertheless, all experimental results were consistent with the calculation results.

3. Conclusion

In this study, we designed a single multi-fold phase metasurface to reconstruct holograms induced by discrete frequency illumination and polarizations. The basic phase holograms were generated using an optimized loop algorithm designed based on the Adam optimization loop. An arbitrary K-fold of the basic phase was reconstructed to display the arbitrary images. The obtained simulation and experimental results satisfied our expectations. The use of selective frequencies and decoupled circular and linear polarization facilitated dynamic modulation to display multi-fold holographic reconstruction. The proposed method does not require nonlinear effects of structures or materials and can conveniently and efficiently achieve multi-fold phase modulation by combining polarization and frequencies. Multi-fold phase modulation induced by frequency and polarization can serve as a novel solution to generating fold phases using a single metasurface for light directional excitation and refraction, orbital angular momentum beam transformation, and other functions. In comparison with the multi-phase modulation based on nonlinear effects, the developed method significantly improves the energy conversion efficiency while reducing the complexity of the experiment. However, owing to the limited range of the selected structure, achieving a strict numerical multi-fold phase wrapping is challenging. This can be addressed by expanding the range of available structures and selecting a method that implements fixed phase elements. The minimum phase matching error is given priority when matching the multiplex phase diagram. This ignores the amplitude constraint to a certain extent, resulting in different light intensity of different channels. By adjusting the intensity ratio of different channel losses reconstructed by the algorithm, the matching amplitude and phase error can be reduced at the same time to select the optimal phase structure. Furthermore, with elaborate design, the developed algorithm can be extended to realize the dynamic orbital angular momentum beam-directed excitation and communication in a device by integrating active materials. Owing to these unique advantages, we believe that the study not only enhances the methods used for multi-fold phase modulation but also presents a foundation for developing potential applications in directional optical communication, light switching, holographic encryption and displays, dynamic optical modulation, and several other fields.

Acknowledgements

National Natural Science Foundation of China Program (62305009). China Postdoctoral Science Foundation (2023M720313).

Conflict of Interest

The authors declare no conflict of interest.

Data Availability Statement

Data underlying the results presented in this paper are not publicly available at this time but may be obtained from the authors upon reasonable request.

Keywords

dynamic encryption, holography, metasurface, multi-fold phase

Received: August 27, 2024
Revised: December 20, 2024
Published online:

[1] X. Li, J. Liu, J. Jia, Y. Pan, Y. Wang, *Opt. Express.* **2013**, *21*, 20577.
[2] X. Wu, H. Zhang, X. Hu, M. Shakeri, C. Fan, J. Ting, *IEEE Robot. Autom. Lett.* **2020**, *5*, 5113.
[3] N. Baek, Y. Lee, T. Kim, J. Jung, S. A. Lee, *APL Photonics.* **2022**, *7*, 116107.
[4] X. Pu, X. Wang, X. Gao, C. Wei, J. Gao, *IEEE Trans. Instrum. Meas.* **2024**, *73*, 5003915.
[5] M. A. Cox, C. Rosales-Guzman, *Appl. Optics.* **2023**, *62*, 7828.
[6] J. Liang, X. Tian, H. Ju, D. Wang, H. Wu, L. Ren, R. Liang, *Opt. Lett.* **2019**, *44*, 4574.
[7] G. Finco, G. Li, D. Pohl, M. Reig Escale, A. Maeder, F. Kaufmann, R. Grange, *Nat. Commun.* **2024**, *15*, 2330.
[8] K. F. Chang, D. M. B. Lesko, C. Mashburn, P. Chang, E. Tsao, A. J. Lind, S. A. Diddams, *Opt. Lett.* **2024**, *49*, 1684.
[9] M. Aburas, P. Bernaudin, A. Drouart, F. Esnault, A. Esper, A. Ghribi, H. Savajols, M. Stodel, *IEEE Trans. Appl. Supercond.* **2024**, *34*, 3700304.
[10] Q. Fan, W. Xu, X. Hu, W. Zhu, T. Yue, F. Yan, P. Lin, L. Chen, J. Song, H. J. Lezec, A. Agrawal, Y. Lu, T. Xu, *Nat. Commun.* **2023**, *14*, 7180.
[11] W. Shi, H. Quan, L. Kong, *Opt. Express.* **2024**, *32*, 3710.
[12] Y. Cheng, L. Zhang, D. Guo, N. Wang, J. Qi, J. Qiu, *IEEE Trans. Ind. Inform.* **2024**, *20*, 8585.
[13] D. Lin, P. Fan, E. Hasman, M. L. Brongersma, *Science.* **2014**, *345*, 298.
[14] G. Zheng, H. Muehlenbernd, M. Kenney, G. Li, T. Zentgraf, S. Zhang, *Nat. Nanotechnol.* **2015**, *10*, 308.
[15] A. V. Kildishev, A. Boltasseva, V. M. Shalaev, *Science.* **2013**, *339*, 1232009.
[16] K. Y. Bliokh, F. J. Rodriguez-Fortuno, F. Nori, A. V. Zayats, *Nat. Photonics.* **2015**, *9*, 796.
[17] G. Ma, M. Yang, S. Xiao, Z. Yang, P. Sheng, *Nat. Mater.* **2014**, *13*, 873.
[18] L. Li, T. J. Cui, W. Ji, S. Liu, J. Ding, X. Wan, Y. B. Li, M. Jiang, C. Qiu, S. Zhang, *Nat. Commun.* **2017**, *8*, 197.
[19] D. Wen, F. Yue, G. Li, G. Zheng, K. Chan, S. Chen, M. Chen, K. F. Li, P. W. H. Wong, K. W. Cheah, E. Y. B. Pun, S. Zhang, X. Chen, *Nat. Commun.* **2015**, *6*, 8241.
[20] E. Arbabi, A. Arbabi, S. M. Kamali, Y. Horie, M. Faraji-Dana, A. Faraon, *Nat. Commun.* **2018**, *9*, 812.
[21] X. Ni, A. V. Kildishev, V. M. Shalaev, *Nat. Commun.* **2013**, *4*, 2807.
[22] J. P. B. Mueller, N. A. Rubin, R. C. Devlin, B. Groever, F. Capasso, *Phys. Rev. Lett.* **2017**, *118*, 113901.
[23] W. Ye, F. Zeuner, X. Li, B. Reineke, S. He, C. Qiu, J. Liu, Y. Wang, S. Zhang, T. Zentgraf, *Nat. Commun.* **2016**, *7*, 11930.
[24] L. Huang, X. Chen, H. Muehlenbernd, H. Zhang, S. Chen, B. Bai, Q. Tan, G. Jin, K. Cheah, C. Qiu, J. Li, T. Zentgraf, S. Zhang, *Nat. Commun.* **2013**, *4*, 2808.
[25] W. T. Chen, A. Y. Zhu, V. Sanjeev, M. Khorasaninejad, Z. Shi, E. Lee, F. Capasso, *Nat. Nanotechnol.* **2018**, *13*, 220.

[26] R. J. Lin, V. Su, S. Wang, M. K. Chen, T. L. Chung, Y. H. Chen, H. Y. Kuo, J. Chen, J. Chen, Y. Huang, J. Wang, C. H. Chu, P. C. Wu, T. Li, Z. Wang, S. Zhu, D. P. Tsai, *Nat. Nanotechnol.* **2019**, *14*, 227.
[27] A. P. Mosk, A. Lagendijk, G. Lerosey, M. Fink, *Nat. Photonics.* **2012**, *6*, 283.
[28] D. Lu, Z. Liu, *Nat. Commun.* **2012**, *3*, 1205.
[29] G. Lee, J. Hong, S. Hwang, S. Moon, H. Kang, S. Jeon, H. Kim, J. Jeong, B. Lee, *Nat. Commun.* **2018**, *9*, 4562.
[30] B. Xu, G. Huang, H. Chen, X. Feng, J. Qiu, K. Luo, L. Peng, D. Liu, P. Han, *Photonics Nanostruct.* **2023**, *53*, 101107.
[31] D. Pan, L. Wan, M. Ouyang, W. Zhang, A. A. Potapov, W. Liu, Z. Liang, T. Feng, Z. Li, *Photonics Res.* **2021**, *9*, 1758.
[32] H. Zhou, C. Zhao, C. He, L. Huang, T. Man, Y. Wan, *Nanophotonics.* **2024**, *13*, 419.
[33] X. Zhang, Y. Zhou, H. Zheng, A. E. Linares, F. C. Ugwu, D. Li, H. Sun, B. Bai, J. G. Valentine, *Nano Lett.* **2021**, *21*, 8715.
[34] A. Saba, M. R. Tavakol, P. Karimi-Khoozani, A. Khavasi, *IEEE Photonics Technol. Lett.* **2018**, *30*, 853.
[35] X. Lin, Y. Rivenson, N. T. Yardimei, M. Veli, Y. Luo, M. Jarrahi, A. Ozcan, *Science.* **2018**, *361*, 1004.
[36] J. Li, D. Mengu, Y. Luo, Y. Rivenson, A. Ozcan, *Adv. Photonics.* **2019**, *1*, 046001.
[37] Y. Luo, D. Mengu, N. T. Yardimci, Y. Rivenson, M. Veli, M. Jarrahi, A. Ozcan, *Light-Science & Applications.* **2019**, *8*,112.
[38] M. S. S. Rahman, T. Gan, E. A. Deger, C. Isil, M. Jarrahi, A. Ozcan, *Nat. Commun.* **2023**, *14*, 6830.
[39] Z. Deng, G. Li, *Mater. Today Phys.* **2017**, *3*, 16.
[40] H. Ren, G. Briere, X. Fang, P. Ni, R. Sawant, S. Heron, S. Chenot, S. Vezian, B. Damilano, V. Brandli, S. A. Maier, P. Genevet, *Nat. Commun.* **2019**, *10*, 2986.
[41] J. Yang, R. Zhao, Z. Meng, J. Li, Q. Wu, L. Huang, A. Zhang, *Photonics Res.* **2022**, *10*, 2607.
[42] Q. Song, X. Liu, C. Qiu, *P. Genevet, Appl. Phys. Rev.* **2022**, *9*, 011311.
[43] J. Yu, S. Park, I. Hwang, D. Kim, F. Demmerle, G. Boehm, M. Amann, M. A. Belkin, J. Lee, *Nat. Photonics.* **2022**, *16*, 72.
[44] N. Nookala, J. Lee, M. Tymchenko, J. S. Gomez-Diaz, F. Demmerle, G. Boehm, K. Lai, G. Shvets, M. Amann, A. Alu, M. Belkin, *Optica.* **2016**, *3*, 283.
[45] F. Walter, G. Li, C. Meier, S. Zhang, T. Zentgraf, *Nano Lett.* **2017**, *17*, 3171.
[46] J. W. Wu, Z. X. Wang, Z. Q. Fang, J. C. Liang, X. Fu, J. F. Liu, H. T. Wu, D. Bao, L. Miao, X. Y. Zhou, Q. Cheng, T. J. Cui, *Adv. Funct. Mater.* **2020**, *30*, 2004144.
[47] M. Wang, Y. Li, Y. Tang, J. Chen, R. Rong, G. Li, T. Cao, S. Chen, *Laser Photon. Rev.* **2022**, *16*, 2200350.
[48] Y. Bao, J. Yan, X. Yang, C. Qiu, B. Li, *Nano Lett.* **2021**, *21*, 2332.
[49] T. Wu, X. Zhang, Q. Xu, E. Plum, K. Chen, Y. Xu, Y. Lu, H. Zhang, Z. Zhang, X. Chen, G. Ren, L. Niu, Z. Tian, J. Han, W. Zhang, *Adv. Opt. Mater.* **2022**, *10*, 2101223.
[50] Z. Li, C. Chen, Z. Guan, J. Tao, S. Chang, Q. Dai, Y. Xiao, Y. Cui, Y. Wang, S. Yu, G. Zheng, S. Zhang, *Laser Photon. Rev.* **2020**, *14*, 2000032.
[51] K. Xu, Y. Liu, X. Fan, X. Wang, X. Yu, Z. Teng, G. Zheng, W. Xiong, H. Gao, *Laser Photon. Rev.* **2024**, 2400815.
[52] M. Q. Mehmood, J. Seong, M. A. Naveed, J. Kim, M. Zubair, K. Riaz, Y. Massoud, J. Rho, *Adv. Sci.* **2022**, *9*, 2203962.
[53] T. Badloe, J. Seong, J. Rho, *Nano Lett.* **2023**, *23*, 6958.
[54] Y. Yin, Q. Jiang, H. Wang, J. Liu, Y. Xie, Q. Wang, Y. Wang, L. Huang, *Adv. Mater.* **2024**, *36*, 2312303.
[55] A. Asad, J. Seong, H. S. Khaliq, J. Lee, Y. Jeon, H. Cabrera, M. Q. Mehmood, L. Gao, H. Kim, J. Rho, *Adv. Funct. Mater.* **2024**, *34*, 2402744.
[56] T. Huang, X. Zhao, S. Zeng, A. Crunteanu, P. P. Shum, N. Yu, *Rep. Prog. Phys.* **2020**, *83*, 126101.